Catalysis Science & Technology

PAPER

View Article Online
View Journal

Cite this: DOI: 10.1039/c4cy01158a

Co_3O_4 particles grown over nanocrystalline CeO_2: influence of precipitation agents and calcination temperature on the catalytic activity for methane oxidation†

H. Wu,[ab] G. Pantaleo,[a] G. Di Carlo,[c] S. Guo,[ab] G. Marcì,[d] P. Concepción,[e] A. M. Venezia[a] and L. F. Liotta*[a]

Received 5th September 2014,
Accepted 30th December 2014

DOI: 10.1039/c4cy01158a

www.rsc.org/catalysis

Crystalline cobalt oxides were prepared by a precipitation method using three different precipitation agents, $(NH_4)_2CO_3$, Na_2CO_3 and $CO(NH_2)_2$. Cobalt oxide nanoparticles corresponding to a Co_3O_4 loading of 30 wt% were also deposited over high-surface area nanocrystalline ceria by the same precipitation agents. The effect of calcination temperature, 350 or 650 °C, on the morphological and structural properties was evaluated. Characterization by BET, XRD, SEM, TEM, Raman spectroscopy, H_2-TPR, XPS and NH_3-TPD was performed and the catalytic properties were explored in the methane oxidation reaction. The nature of the precipitation agent strongly influenced the textural properties of Co_3O_4 and the Co_3O_4–CeO_2 interface. The best control of the particle size was achieved by using $CO(NH_2)_2$ that produced small and regular crystallites of Co_3O_4 homogeneously deposited over the CeO_2 surface. Such a Co_3O_4–CeO_2 system precipitated by urea showed enhanced low-temperature reducibility and high surface Co^{3+} concentration, which were identified as the key factors for promoting methane oxidation at low temperature. Moreover, the synergic effect of cobalt oxide and nanocrystalline ceria produced stable full conversion of methane in the entire range of investigated temperature, up to 700–800 °C, at which Co_3O_4 deactivation usually occurs.

1. Introduction

Cobalt oxide catalysts have been extensively investigated during the last two decades as possible substitutes for precious metals due to their catalytic properties in several oxidation reactions for waste gas abatement[1–11] and diesel soot combustion.[12,13] Recently growing scientific attention has been paid to Co_3O_4-based oxides as highly efficient catalysts for the complete abatement of unburned methane released from natural gas vehicles (NGVs). To this aim, different combinations of Co_3O_4 and various oxide supports have been proposed.[5,14,15] Highly dispersed Co_3O_4 particles promoted by ZrO_2 have been claimed as active sites for methane oxidation over catalysts with low cobalt content.[5] Nanosized Co_3O_4/γ-Al_2O_3 catalysts with a defective structure, prepared by a combination of wetness impregnation and combustion synthesis, exhibited high activity for the total oxidation of methane.[14] The promotional effect on methane oxidation of manganese doped cobalt oxides was ascribed to crystal defects in the spinel structure of Co_3O_4, which probably resulted in an increased amount of Co^{2+} ions responsible for the catalytic activity.[15]

CoO_x–CeO_2 systems have been widely employed in the few last years for different applications, depending on the Co–Ce composition, the preparation method and the nature of pre-treatments.[8,16–19] We have reported that Co_3O_4–CeO_2 coprecipitated oxides are effective catalysts for methane oxidation in the presence of a stoichiometric oxygen concentration and the best activity was attained at a Co/Ce atomic ratio of ~1.[20,21] In this sample, the presence of highly dispersed Co_3O_4 particles in good contact with CeO_2 was claimed as the key factor for the improved redox properties and catalytic

[a] Istituto per lo Studio dei Materiali Nanostrutturati (ISMN), Consiglio Nazionale delle Ricerche (CNR), Via Ugo La Malfa 153, 90146, Palermo, Italy. E-mail: liotta@pa.ismn.cnr.it; Fax: +39 091 6809399; Tel: +39 091 6809371
[b] Department of Applied Physics, Northwestern Polytechnical University (NPU), Youyi Xilu 127, 710072, Xi'an, Shaanxi, PR China
[c] Istituto per lo Studio dei Materiali Nanostrutturati (ISMN), Consiglio Nazionale delle Ricerche (CNR), Via Salaria km 29300, 00015 Monterotondo Stazione, Roma, Italy
[d] "Schiavello-Grillone" Photocatalysis Group, Dipartimento di Energia, Ingegneria dell'Informazione e Modelli Matematici (DEIM), Università di Palermo, Viale delle Scienze, 90128 Palermo, Italy
[e] Instituto de Tecnología Química, UPV-CSIC, Campus de la Universidad Politécnica de Valencia, Avenida de los Naranjos s/n, 46022 Valencia, Spain

† Electronic supplementary information (ESI) available. See DOI: 10.1039/c4cy01158a

performance. High lattice oxygen mobility and formation of surface anionic vacancies in such a Co_3O_4–CeO_2 system were also relevant to propene and toluene oxidation activity.[22,23]

On these grounds, Co_3O_4-based catalysts are definitely good candidates for oxidation reactions; however, deactivation processes induced by high temperature, such as loss of surface area, thermal decomposition to the less active CoO and interactions of cobalt with the matrix leading to inactive phases (*i.e.*, $CoAl_2O_4$, $CoTiO_3$, $CoZr_3O_{0.69}$), limit its application at high temperatures.[5,21,24,25]

Therefore, deposition of Co_3O_4 active sites over a high surface area carrier is attractive to achieve high catalytic performance and long-term stability.

It has been reported that the properties of cerium oxide can change drastically when the particle size is decreased to the nanosize region, becoming a very active support that strongly interacts with gold.[26,27] It was, therefore, clear to us that such nanocrystalline ceria would be a good candidate for the deposition of Co_3O_4 nanoparticles.

The preparation of Co_3O_4 nanocrystals with different morphology is widely documented, with the morphology strongly dependent on the experimental conditions, reaction temperature, and nature of the precipitation agent.[11,28–31] Synthesis of Co_3O_4 nanoparticles with a small diameter, in the range of 20–40 nm, has been carried out by homogeneous precipitation of cobalt hydroxide carbonate with urea at 110 °C starting from a cobalt nitrate precursor.[29] The synthesis procedures also allowed the control of the crystal shape and crystal orientation plane which have been claimed as key factors for the CO and CH_4 oxidation activity of Co_3O_4 nanocrystals.[11,31]

The present work focuses on the effect of the precipitation agents, Na_2CO_3, $(NH_4)_2CO_3$, and $CO(NH_2)_2$, on the nature of the cobalt species, cobalt hydroxide carbonate and/or Co_3O_4, detected after drying the powder at 120 °C. Their successive thermal conversion to crystalline Co_3O_4 spinel and the influence of the calcination temperature and duration time, 350 °C for 3 h or 650 °C for 5 h, on the physicochemical properties were investigated. The influence of nanocrystalline ceria as a support on the cobalt species' growth and crystallization was also investigated by preparing three mixed oxides using sodium-, ammonium carbonate and urea with the composition Co_3O_4(30 wt%)–CeO_2. The so obtained oxides were characterized by BET, XRD, SEM, TEM, Raman spectroscopy, H_2-TPR, XPS and NH_3-TPD techniques. The catalytic properties were evaluated for methane oxidation in the presence of a stoichiometric oxygen concentration.

2. Experimental

All chemicals (Sigma-Aldrich) were of analytical grade and were used as received without further purification.

2.1. Synthesis of nanocrystalline CeO_2

A colloidal dispersion of CeO_2 nanoparticles was prepared by thermolysis of an acidified $Ce(NO_3)_4$ solution followed by re-dispersion, according to a previously described method.[26,27] The dispersion consisting of discrete CeO_2 nanoparticles that display a spherical morphology was purified and concentrated using an ultra-filtration cell equipped with a 3KD membrane. The purification was monitored by the residual acidity of the dispersion, determined by acid titration of the supernatant after ultra-centrifugation at 50 000 rpm for 6 h. After evaporation in air at room temperature, the resulting solid sample was calcined at 500 °C for 6 h using a programmable oven; heating in air at a rate of 1 °C min^{-1} was performed in order to favour complete crystallization of the fluorite structure, according to the published procedure.[26,27]

2.2. Synthesis of Co_3O_4 and Co_3O_4(30 wt%)–CeO_2 oxides

Bare Co_3O_4 oxides were prepared by a precipitation method with three different precipitation agents, Na_2CO_3, $(NH_4)_2CO_3$ and $CO(NH_2)_2$, starting from $Co(NO_3)_2{\cdot}6H_2O$ as the cobalt precursor. In a typical preparation for obtaining 2 g of the Co_3O_4 oxide, Na_2CO_3 or $(NH_4)_2CO_3$ solution (0.5 M) was added drop by drop, under mild heating at 80 °C, to a suitable volume of cobalt nitrate water solution (1 M) until pH = 8.5. The as formed precipitate was aged overnight in the mother liquor at a constant temperature of 80 °C. The third preparation was carried out using a homogeneous precipitation method by urea hydrolysis under stirring at 90 °C overnight. In this method urea in excess (molar ratio: urea/cobalt nitrate = 100) was added. The obtained solid, labeled as Co_{Na}, Co_{NH_4} and Co_{urea}, was filtered and washed with distilled water several times until neutrality. Then it was dried overnight at 120 °C in an oven, then divided into two portions and calcined in static air at 350 °C for 3 h or at 650 °C for 5 h (heating rate 3 °C min^{-1}) in order to form crystalline Co_3O_4 spinel.

By the same precipitation method with three agents, Co_3O_4 with a loading of 30 wt% was deposited over nanocrystalline CeO_2. Drying at 120 °C and calcination at 350 °C and at 650 °C were performed as described above. The obtained oxides were labeled as $Co30Ce_{Na}$, $Co30Ce_{NH_4}$ and $Co30Ce_{urea}$. For all samples herein discussed the drying or calcination temperature is added as a subscript to the name label (*i.e.* Co_{Na350} and $Co30Ce_{Na350}$ refer to bare Co_3O_4 and Co_3O_4(30 wt%)/CeO_2 precipitated by Na_2CO_3 solution and calcined at 350 °C).

2.3. Characterization

Specific surface area (SSA) measurements were performed using a Sorptomatic 1900 (Carlo Erba Instruments), by physical adsorption of N_2 at the temperature of liquid nitrogen (−196 °C), using the BET method in the standard pressure range of 0.05–0.30 p/p_0.[32]

X-ray diffraction (XRD) patterns were recorded with a D5005 X-ray diffractometer (SIEMENS) using Cu Kα radiation coupled with a graphite monochromator. The assignment of the various crystalline phases was based on the Inorganic Crystal Structure Database (ICSD, FIZ Karlsruhe).[33] The mean

crystallite size (d) of the Co_3O_4 phase was calculated from the line broadening of the most intense reflection using the Scherrer equation.[34] The estimated error was ±10%.

Scanning electron microscopy (SEM) images and energy-dispersive X-ray (EDX) analyses were obtained using a FEI Quanta 200 ESEM microscope operating at 20 kV from the specimens after being coated with a thin layer of gold.

TEM images were obtained with a Philips CM10 microscope operating at 100 kV. A portion of the ground solid was suspended in CH_2Cl_2 and sonicated for 1 min. Then, a drop was extracted under sonication and deposited onto a copper grid and dried before observation.

Raman spectra were acquired with a Renishaw Raman inVia spectrometer equipped with a Leika DM LM microscope and a 785 nm HPNIR diode laser as an excitation source. The laser power on the sample was 30 mW. A 50× objective of 8 mm optical length was used to focus the depolarized laser beam onto a 3–5 μm spot on the sample surface and to collect backscattered light. The Raman scattering was collected in static-scan mode in the 100–3000 cm^{-1} spectral region with a resolution better than 4 cm^{-1}. Ten scans were accumulated for each spectrum during a total scanning time of 100 s.

Temperature-programmed reduction (TPR) experiments were carried out with a Micromeritics Autochem 2910 apparatus equipped with a thermal conductivity detector (TCD). In the TPR experiments, a gas mixture H_2 (5 vol.% in Ar, 30 ml min^{-1}) was flowed over the sample pre-treated with O_2 (5 vol.% in He) at 550 °C for 30 min, heating from room temperature to 1000 °C (rate: 10 °C min^{-1}). In order to avoid any influence of mass transfer effects on the shape of the TPR profiles, the absence of inter- and intra-particle mass transfer limitations was accurately checked.

The acidity of the oxide catalysts was determined by temperature-programmed desorption of ammonia (NH_3-TPD) experiments by using a Micromeritics Autochem 2910 apparatus equipped with a thermal conductivity detector (TCD) and a mass quadrupole spectrometer (ThermoStar, Balzers). A sample amount of 0.3 g was pre-treated in He flow at 200 °C for 1 h. Then, after cooling down to room temperature, ammonia adsorption was performed by flowing 5% NH_3/He stream (30 ml min^{-1}) for 1 h. In order to remove all physically adsorbed ammonia, the sample was purged by flowing 100 ml min^{-1} He at 100 °C for 1 h, then after cooling down to room temperature, ammonia desorption was started by flowing He (30 ml min^{-1}) and heating up to 500 °C (rate: 10 °C min^{-1}), holding time at 500 °C for 30 min. All of the gases desorbed from the sample were monitored by online TCD and QMS analysis. The total acidity of the catalyst was calculated by integration of the NH_3 desorption profile referred to the QM signal, at mass 17.

The X-ray photoelectron spectroscopy analyses were performed with a VG Microtech ESCA 3000 Multilab, equipped with a dual Mg/Al anode. The spectra were excited by the unmonochromatised Al Kα source (1486.6 eV) run at 14 kV and 15 mA. The analyser operated in the constant energy (CAE) mode. For the individual peak energy regions, a pass energy of 20 eV set across the hemispheres was used. Survey spectra were measured at 50 eV pass energy. The sample powders were studied as pellets, mounted on double-sided adhesive tape. The pressure in the analysis chamber was in the range of 10^{-8} Torr during data collection. The constant charging of the samples was removed by referencing all of the energies to C 1s set at 285.1 eV, arising from the adventitious carbon. The invariance of the peak shapes and widths at the beginning and at the end of the analyses ensured the absence of differential charging. Analyses of the peaks were performed with the software provided by VG, based on a non-linear least squares fitting program using a weighted sum of Lorentzian and Gaussian component curves after background subtraction according to Shirley and Sherwood.[35,36] Atomic concentrations were calculated from the peak intensity using the sensitivity factors provided with the software. The binding energy values are quoted with a precision of ±0.15 eV and the atomic percentage with a precision of ±10%.

2.4. Catalytic tests

Methane combustion catalytic tests were performed under stoichiometric conditions by flowing a gas reaction mixture consisting of 0.3 vol.% CH_4 and 0.6 vol.% of O_2 in He ($\lambda = 1$).[20] The experiments were carried out over 50 mg of the catalyst (fraction sieved between 180 and 250 μm) at a flow rate of 50 ml min^{-1} (STP), equivalent to a weight hourly space velocity (WHSV) of 60 000 ml g^{-1} h^{-1} by using a quartz U-shaped reactor with an inner diameter of 12 mm electrically heated in a furnace. The reaction temperature was monitored by a K-type thermocouple in contact with the catalytic bed (length, 12 mm). Before the catalytic tests the samples were pre-treated "*in situ*" under flowing O_2 (5 vol.% in He) at 350 °C for 1/2 h. The activities were measured by increasing the temperature from 200 to 600 or 800 °C by steps of 50 °C, a holding time of 30 min at each temperature. The catalysts calcined at 350 °C have been tested up to 600 °C, while the samples calcined at 650 °C were investigated up to 800 °C. The inlet and outlet gas compositions were analyzed by an online mass quadrupole spectrometer (ThermoStar™, Balzers) in order to follow the evolution of all the species, CH_4, CO, CO_2, H_2, H_2O, and O_2. Moreover, the concentration of the CO and CO_2 species was determined by an IR analyser (ABB Uras 14), calibrated in the range of 0–3000 ppm for CO and 0–10 000 ppm for CO_2. The reaction products of methane oxidation were CO_2 and H_2O; no significant CO (max 10 ppm) was detected in the overall range of temperature. The carbon balance was close to ±5% in all of the catalytic tests.

3. Results and discussion

3.1. Structural and textural properties of the catalysts

Fig. 1 shows the powder XRD patterns of the as-prepared cobalt oxides species dried at 120 °C. The weak diffraction intensities of Co_{Na120} indicate that such a sample prepared

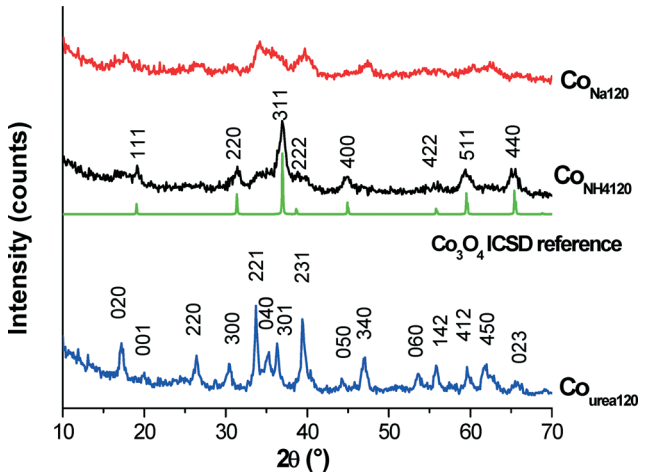

Fig. 1 XRD patterns of cobalt hydroxide carbonate and/or Co_3O_4 species prepared by the precipitation method using three different precipitating agents and dried at 120 °C.

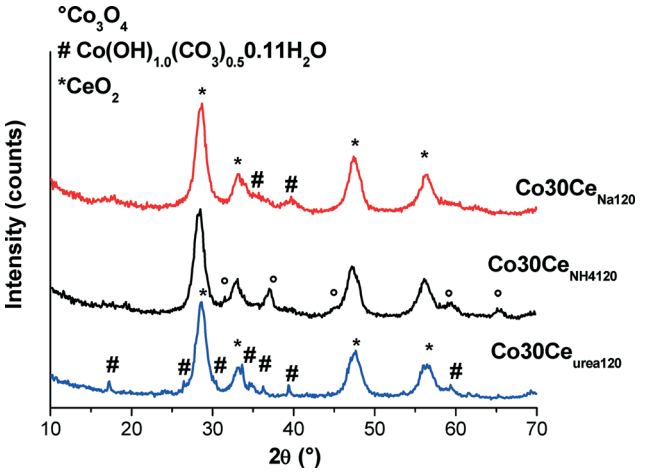

Fig. 2 XRD patterns of cobalt hydroxide carbonate and/or Co_3O_4 species over nanocrystalline CeO_2 deposited by the precipitation method using three different precipitating agents and dried at 120 °C.

by precipitation with Na_2CO_3 solution is not well crystallized. $Co_{urea120}$ shows better crystallinity and peaks characteristic of the orthorhombic cobalt hydroxide carbonate phase, $Co(OH)_{1.0}(CO_3)_{0.5}{\cdot}0.11H_2O$, in good agreement with the literature data.[29,31] The *hkl* reflections shown in Fig. 1 can be indexed perfectly to this phase. Surprisingly, diffraction peaks typical of the Co_3O_4 fcc phase (space group *Fd3m*) at 2θ = 19.0°, 31.3°, 37.0°, 38.6°, 44.9°, 55.8°, 59.4° and 65.4°, corresponding to the (111), (220), (311), (222), (400), (422), (511) and (440) crystal planes,[33] were observed in the XRD pattern of the Co_{NH_4120} sample. The low-crystalline features of the cobalt hydroxide carbonate species were also identified as the main background components. In a previous study[37] where $(NH_4)_2CO_3$ was used as the precipitation agent, cobalt hydroxide carbonate was obtained as the only compound. The crystallization of Co_3O_4 occurring under our experimental conditions could be ascribed to the longer ageing procedure at 80 °C herein employed that could favour $Co^{2+} \rightarrow Co^{3+}$ oxidation.

In Fig. 2 the powder XRD patterns of the cobalt species precipitated over nanocrystalline CeO_2 and dried at 120 °C are displayed. Compared with the powder XRD patterns of bare cobalt hydroxide carbonate and Co_3O_4 compounds, the presence of CeO_2 does not seem to affect the nature of such species, especially for samples precipitated by $(NH_4)_2CO_3$ and $CO(NH_2)_2$, wherein weakly crystalline peaks of Co_3O_4 and of the orthorhombic cobalt hydroxide carbonate phase were detected, respectively. The pattern of $Co30Ce_{Na120}$ mainly shows CeO_2 signals, although small features of the cobalt hydroxide carbonate species can be seen. By comparing Fig. 1 and 2, the effect of ceria on the dispersion of the cobalt phases can be noted.

After calcination at 350 °C all cobalt phases crystallized into Co_3O_4, as detected by XRD for the bare cobalt oxides and as well for the Co30Ce samples. Calcination at higher temperature, 650 °C, makes the Co_3O_4 peaks sharper, in particular, for the Co_{NH_4} sample. In Fig. 3a–b, the powder XRD patterns of the bare cobalt oxides after calcination at 350 and 650 °C are shown. The same trend is observed for the Co30Ce catalysts after calcinations (see Fig. S1†), although nanocrystalline ceria plays a fundamental role in

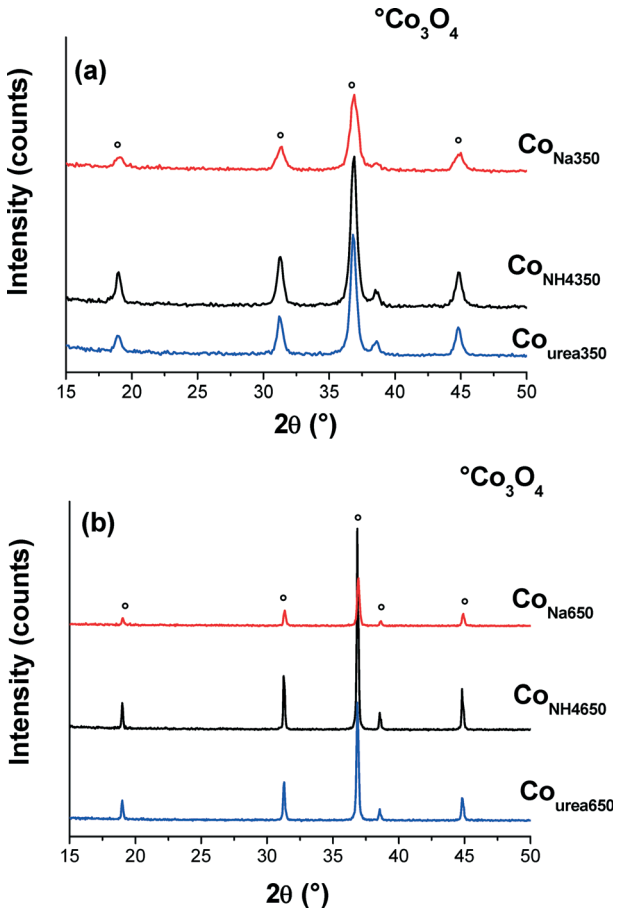

Fig. 3 XRD patterns of bare Co_3O_4 oxides, prepared by the precipitation method using three different precipitating agents, after calcination at (a) 350 °C and (b) 650 °C.

maintaining supported Co_3O_4 crystallites that are better dispersed than those obtained using bare oxides. These results indicate that the crystal phases (cobalt hydroxide carbonate and/or Co_3O_4) formed by the precipitation method are related to the used precipitant. Moreover, the crystallinity is also function of the precipitation agent; the sharpest diffraction peaks of the Co_3O_4 spinel phase were observed for the Co_{NH_4} and $Co30Ce_{NH_4}$ samples.

The mean crystallite sizes (d) of the Co_3O_4 phase calculated from the (311) diffraction line are shown in Table 1 for the Co and Co30Ce series calcined at 350 and 650 °C. For samples calcined at 350 °C the d values range between 10 and 25 nm. For both series calcination at 650 °C caused pronounced sintering of crystallites, in particular for samples precipitated by $(NH_4)_2CO_3$. Those prepared by Na_2CO_3 and $CO(NH_2)_2$ maintained relatively smaller sizes, between 40 and 110 nm. Nanocrystalline CeO_2 stabilized significantly the Co_3O_4 particles against sintering, in particular $Co30Ce_{urea650}$ and $Co30Ce_{Na650}$. Moreover, perusal of Table 1 reveals a less pronounced increase of the d values for the $Co30Ce_{650}$ samples as compared to the corresponding Co_{650} series, especially for Co_3O_4 precipitated in the presence of sodium carbonate and urea, suggesting the highest stabilizing effect of nanocrystalline ceria for those samples.

Similar to the trend found for the Co_3O_4 crystallite sizes, the BET surface area values for the bare cobalt oxides and for the Co30Ce samples depend on the precipitation agent and decreased by increasing the calcination temperature from 350 to 650 °C, as shown in Table 1. All Co30Ce samples calcined at 350 °C have a specific surface area higher than 100 $m^2\ g^{-1}$ that diminished to about half for those calcined at 650 °C. The specific surface area of nanocrystalline CeO_2 was equal to 198 $m^2\ g^{-1}$. The Co_3O_4 oxides treated at 350 °C showed a surface area around 30–40 $m^2\ g^{-1}$ and suffered stronger thermal shrinkage than the ceria-supported oxides, with the BET values decreasing to ~5–10 $m^2\ g^{-1}$ upon calcination at 650 °C.

In order to have a better understanding of the morphological and structural differences between the various samples prepared by different precipitation agents a careful microscopy investigation by SEM and TEM analysis was performed on all of the samples.

In Fig. 4 the SEM images of nanocrystalline CeO_2, Co_3O_4 and Co30Ce samples calcined at 350 °C and precipitated by $(NH_4)_2CO_3$ and by urea are shown. CeO_2 powder shows uniform morphology and appears to be constituted of nanoparticles *ca.* 25 nm in size agglomerated into nearly spherical particles *ca.* 3 μm in diameter (Fig. 4a–b). The shape of the bare oxides, $Co_{urea350}$ and Co_{NH_4350} is different. $Co_{urea350}$ consists of homogeneous nanorod-shaped particles with a size between 30 and 50 nm, while for Co_{NH_4350} inhomogeneously agglomerated nanoparticles were detected (Fig. 4c–d). SEM observation of $Co30Ce_{urea350}$ evidenced that CeO_2 nanoparticles are homogenously covered by nanorod-shaped particles, indicating that precipitation by urea ensures the controlled growth of Co_3O_4 nanoparticles onto the CeO_2 surface (Fig. 4e). On the other hand, $Co30Ce_{NH_4350}$ failed to show a uniform distribution of Co_3O_4 nanoparticles over ceria (Fig. 4f). EDX analyses confirmed the so far discussed data, indicating that for $Co30Ce_{urea350}$ the average atomic percentage of Co is slightly higher (59 ± 10) than the nominal one (48); consequently, the average atomic percentage of Ce (41 ± 10) is slightly lower than the nominal value (52). However, the values are quite reproducible on different agglomerates present in a large area of ~500 μm per side. Conversely Co and Ce were quite heterogeneously distributed from agglomerate to agglomerate for $Co30Ce_{NH_4350}$ with the atomic percentages of Co and Ce highly fluctuating with respect to the nominal values. Based on the reported data, we have considered it worthy of interest to focus our attention on the $Co30Ce_{urea}$ sample and to investigate the effect of

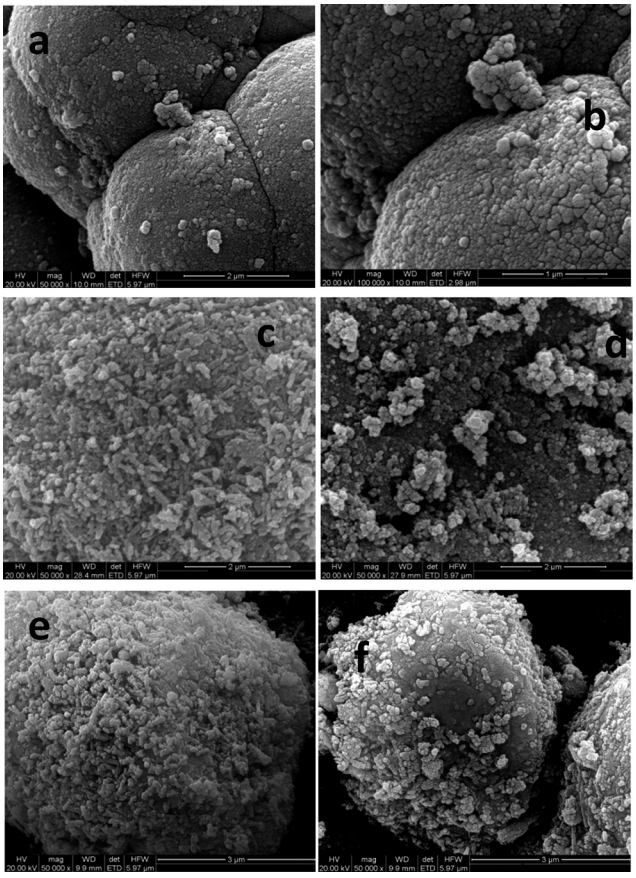

Fig. 4 SEM images of (a), (b) nanocrystalline CeO_2; (c) $Co_{urea350}$; (d) Co_{NH_4350}; (e) $Co30Ce_{urea350}$; and (f) $Co30Ce_{NH_4350}$.

Table 1 Mean crystallite size of the Co_3O_4 phase and the specific surface area of all the prepared samples, bare Co_3O_4 and Co30Ce oxides

Sample	d (nm)	BET surface area ($m^2\ g^{-1}$)	Sample	d (nm)	BET surface area ($m^2\ g^{-1}$)
$Co_{urea350}$	19.0	37.0	$Co30Ce_{urea350}$	14.0	122.0
Co_{Na350}	16.0	43.0	$Co30Ce_{Na350}$	10.0	127.0
Co_{NH_4350}	24.0	31.0	$Co30Ce_{NH_4350}$	19.0	108.0
$Co_{urea650}$	110.0	8.0	$Co30Ce_{urea650}$	61.0	53.0
Co_{Na650}	72.0	10.0	$Co30Ce_{Na650}$	40.0	64.0
Co_{NH_4650}	145.0	5.9	$Co30Ce_{NH_4650}$	121.0	47.0

the temperature of treatment, *i.e.*, 120, 350 and 650 °C, on the morphological properties. In Fig. 5, the SEM micrographs are shown. After drying at 120 °C the $Co30Ce_{urea}$ sample consists of well defined nanorods with a diameter of around 20 nm and a length ranging from 500 nm up to about 1.5 μm. Such morphology is typical of cobalt hydroxide carbonates, as previously reported.[31] The sample calcined at 350 °C maintains the rod-like morphology but the nanorods are much shorter (maximum length ~500 nm) with a particle size between 30 and 50 nm that further increased up to 60–80 nm after calcination at 650 °C.

Fig. 6 shows the TEM images corresponding to the nanocrystalline CeO_2 support. Very small crystallites, with an average size below 10 nm, can be observed. In Fig. 7 the TEM images of Co_{urea} calcined at 350 °C and 650 °C are displayed. In accordance with the literature[29] Co_3O_4 shows a bead-like structure with nanoparticles interconnected along the longitudinal directions of the rods. The increase of the crystallite size with increasing calcination temperature is clearly evidenced and in agreement with the particle sizes (d) of the Co_3O_4 phase calculated by the Scherrer equation (see Table 1).

The TEM images of Co30Ce catalysts prepared by precipitation with Na_2CO_3, $(NH_4)_2CO_3$ and $CO(NH_2)_2$ and calcined at 350 °C are compared in Fig. 8. $Co30Ce_{Na}$ and $Co30Ce_{NH_4}$ appear to be quite heterogeneous, with large agglomerations of CeO_2 particles, which are not directly interacting with the Co_3O_4 crystallites (Fig. 8a–d). This effect is more evident in the case of $Co30Ce_{NH_4}$ characterized by bigger Co_3O_4 crystallites (Fig. 8c–d). Both features are in agreement with the Raman results reported below.

When the precipitation of Co_3O_4 was carried out using urea with calcination at 350 °C, we observed a much more homogeneous distribution of the Co_3O_4 and CeO_2 particles, a better interaction between these oxides and a small particle size (15–25 nm) (Fig. 8e–f). The higher degree of homogeneity of these materials detected by TEM is in agreement with the Raman results. After calcination at 650 °C larger Co_3O_4 crystals were obtained resulting in segregation from the ceria support, in particular for $Co30Ce_{NH_4}$, undergoing sintering to form crystallites bigger than 100 nm, while for $Co30Ce_{urea}$

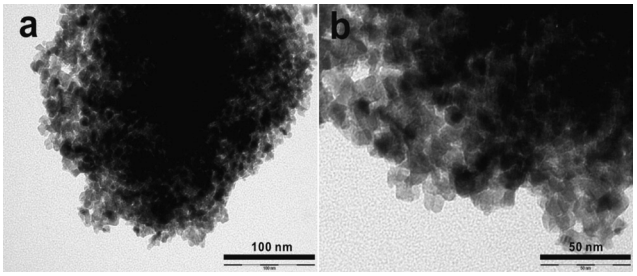

Fig. 6 TEM images of nanocrystalline CeO_2.

the crystal size was smaller and the perimeter interface Co_3O_4–CeO_2, regarded as a fundamental parameter in catalysis, was still clearly detectable (see Fig. S2†).

To further analyze the structure of Co_3O_4 and Co30Ce oxides as a function of the precipitation agent and calcination temperature, the Raman spectra have been registered. In Fig. S3† the Raman spectra corresponding to Co_{Na350}, Co_{NH_4350} and Co_{urea} calcined at 350 and 650 °C are displayed. In all cases the five characteristic bands assigned to the active modes of the Co_3O_4 spinel crystalline phase[38,39] were observed. No additional bands, corresponding to other phases, such as CoO, were found.[40] Fig. S4† shows the spectra obtained for $Co30Ce_{Na}$, $Co30Ce_{NH_4}$ and $Co30Ce_{urea}$ calcined at 350 °C. In order to investigate the effect of the calcination temperature, the spectrum of $Co30Ce_{urea650}$ is also reported. Four different spectra are presented for each sample, corresponding to different mappings carried out during spectra collection, in order to show the possible heterogeneity of the materials.

Compared with Fig. S3† we can see that the bands corresponding to the spinel structure of Co_3O_4 are still present, and an additional band appears at around 460 cm^{-1}, slightly before, or in some cases even overlapping the band corresponding to the E_g Raman active mode of Co_3O_4. This band has been assigned to the F_{2g} Raman active mode of the fluorite structure of CeO_2, and its intensity is known to decrease significantly with Co loading.[41]

In the case of the sample prepared by precipitation with Na_2CO_3, the Co_3O_4 bands are considerably broad, in

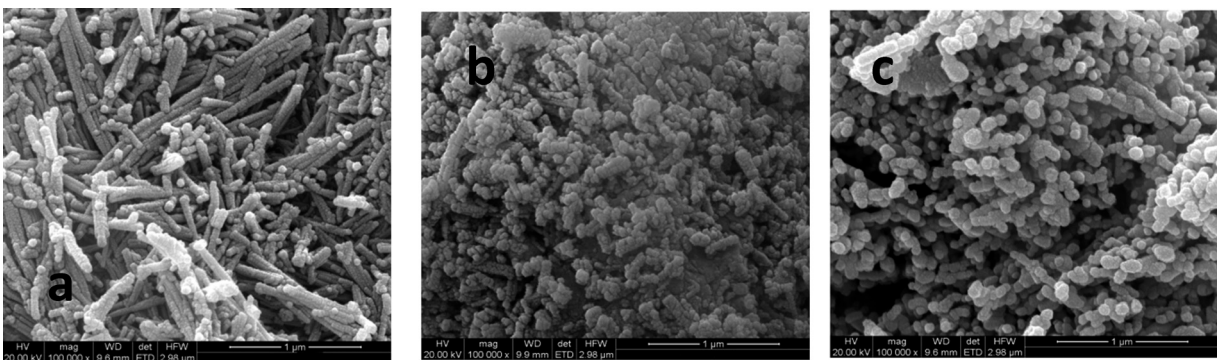

Fig. 5 SEM images of $Co30Ce_{urea}$ treated at different temperatures: (a) 120 °C, (b) 350 °C, and (c) 650 °C.

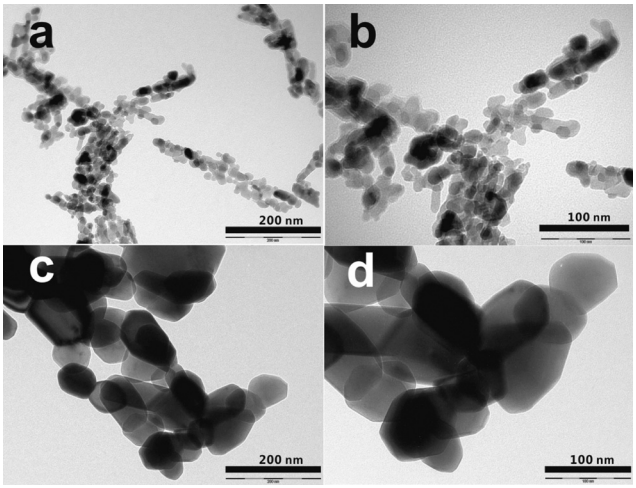

Fig. 7 TEM images (a, b) of Co_{urea} calcined at 350 °C and (c, d) Co_{urea} calcined at 650 °C.

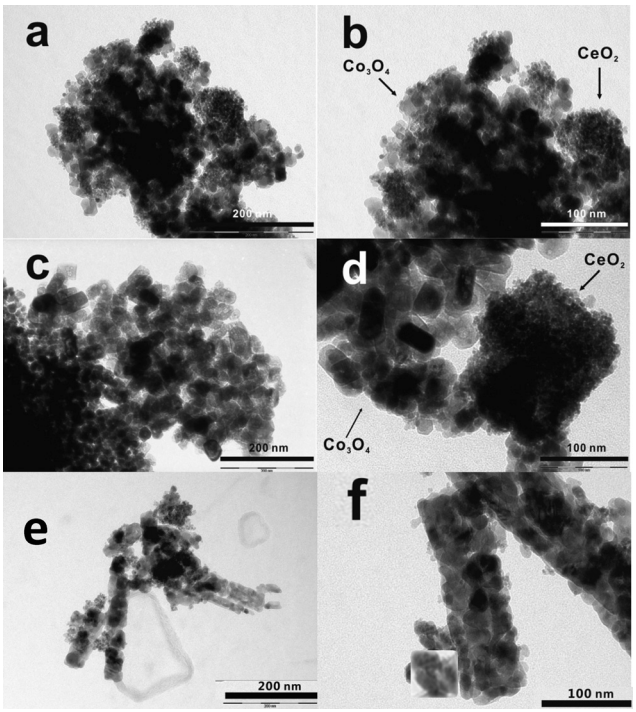

Fig. 8 TEM images of (a, b) $Co30Ce_{Na350}$, (c, d) $Co30Ce_{NH_4350}$, and (e, f) $Co30Ce_{urea350}$.

accordance with the presence of small crystallites, and the spectra differ from one map to the other (see Fig. S4a†). In fact, the Co_3O_4 bands are almost absent in the red spectrum corresponding to map2, whereas the green spectrum (map3) does not present the band assigned to CeO_2.

When $(NH_4)_2CO_3$ is used as the precipitation agent (see Fig. S4b†), sharper and more intense bands appeared for the Co_3O_4 phase, and a small CeO_2 peak appeared only in one of the maps (map4).

The sample prepared by means of urea (see Fig. S4c†) presents broad but more intense Co_3O_4 bands than in the case of Na_2CO_3, and the CeO_2 band at 460 cm^{-1} can hardly be detected as a shoulder of the E_g Co_3O_4 phonon mode, and only in two of the spectra (maps 2 and 3). Based on the smaller differences between the different mappings it can be concluded that this sample is more homogeneous. These properties are maintained after calcination of the $Co30Ce_{urea650}$ sample (Fig. S4d†). The above reported Raman results confirm XRD, SEM and TEM data.

3.2. Temperature-programmed reduction

High bulk oxygen mobility (through the Mars–van Krevelen mechanism) and formation of highly active oxygen species activated by oxygen vacancies are widely recognized as the main factors influencing the catalytic activity of Co_3O_4 and Co*x*Ce for CO, CH_4 and VOC catalytic oxidation.[42] In order to gain insight into the effect of different precipitation agents and as well the interaction between Co_3O_4 and CeO_2 on the reduction properties, H_2-TPR experiments were performed on the prepared Co_3O_4 and Co30Ce oxides. In Fig. 9 the reduction curves are shown. With respect to the reduction process of Co_3O_4, there are various controversial viewpoints. Arnoldy and Moulijn reported one broad peak for the reduction of Co_3O_4.[43] A single reduction peak at 434 °C was also found by Luo *et al.*[44] However, more commonly the reduction of Co_3O_4 is described as a two-step process involving the intermediate reduction of CoO.[42] These different results could be explained by considering that the reduction behaviour of Co_3O_4 is highly dependent on the preparation method and dispersion of the particles. Large particles are usually reduced to metallic cobalt in a single step, while for nanoparticles a two-step process often occurs.[18,45,46] Two reduction peaks, labelled as peak I and peak II, in the temperature range of ~200–400 °C, were detected in the TPR profiles of the prepared Co_3O_4 oxides calcined at 350 and at 650 °C (see Fig. 9a, b). Confirming our previous data and in agreement with other literature results, peak I was associated with the reduction of Co^{3+} to Co^{2+} and peak II was ascribed to the reduction of CoO to metallic cobalt.[20,47,48] For a given calcination temperature, 350 or 650 °C, moving from Co_{Na} having small particles to Co_{NH_4} characterized by bigger crystallites, both reduction peaks shifted to higher temperature, indicating decreased reducibility. Moreover, increasing the calcination temperature from 350 to 650 °C produced a further shift to higher temperature. Larger Co_3O_4 crystallites and lower BET surface areas (Table 1) induced by the calcinations at 650 °C can account for the decreased reducibility. Independent of the preparation method and the calcination temperature, the overall hydrogen consumption related to the area of the two peaks (Fig. 9a, b) was equal to 370 ± 5 ml. With the theoretical H_2 consumption for the total reduction of Co_3O_4 to Co^0 equal to ~406 ml H_2 g^{-1} (calculated at 1 atm and 298 K) the measured value is within the experimental error (±10%).

The TPR profiles of the Co30Ce oxides calcined at 350 °C (Fig. 9c) are characterized by two to three main reduction

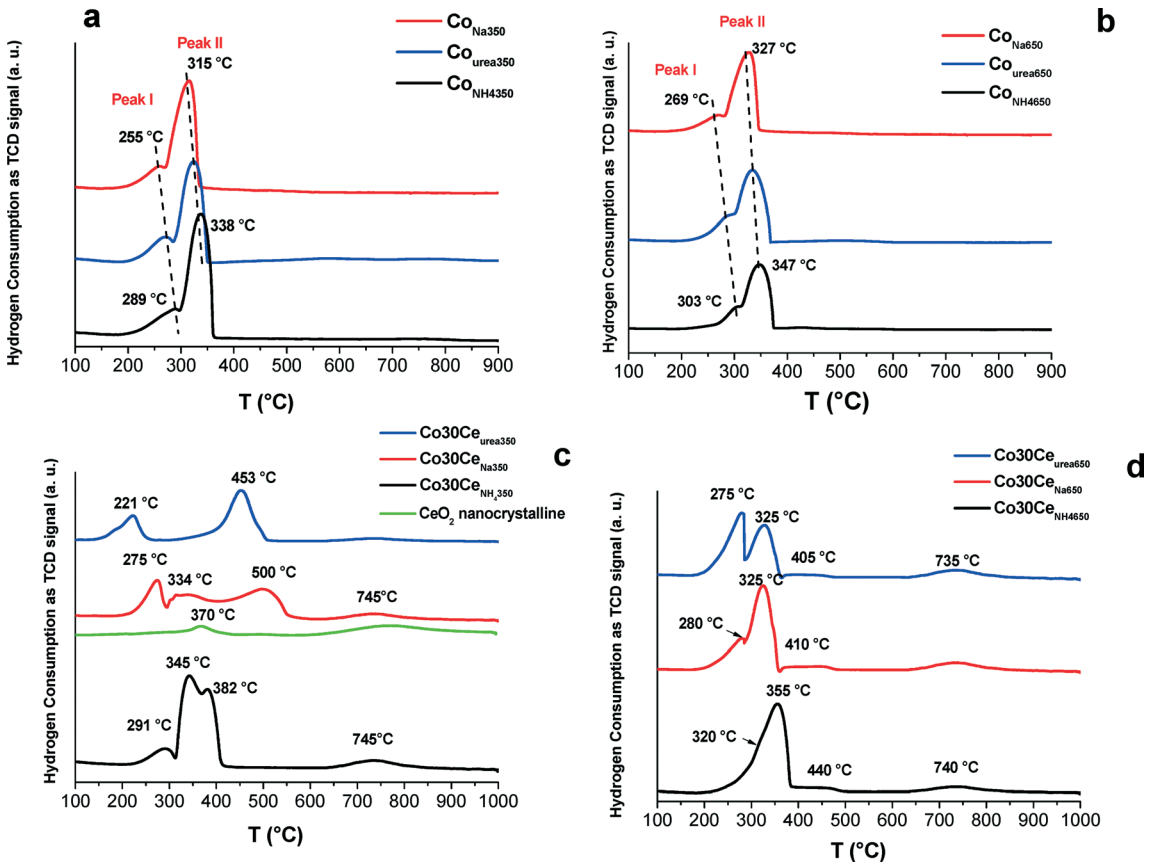

Fig. 9 H_2-TPR profiles of (a, b) bare Co_3O_4 and (c, d) Co30Ce catalysts prepared by the precipitation method using three different precipitating agents and calcined at 350 or at 650 °C.

peaks in the range of temperature between 150 and 600 °C. An additional peak at about 740 °C is present in all of the reduction profiles. The $Co30Ce_{urea}$ sample exhibited the highest reducibility at low temperature with a peak centred at 221 °C having a shoulder at 183 °C and a second intense peak at 453 °C. For $Co30Ce_{Na}$ the reduction occurs in a wide range of temperature, with three broad signals centred at 275, 334 and 500 °C. For $Co30Ce_{NH_4}$ characterized by larger Co_3O_4 particles, reduction is completed in a shorter range of temperature with three close peaks at 291, 345 and 382 °C. In Fig. 9c the reduction profile of nanocrystalline ceria is also reported for comparison. Two main hydrogen consumptions, at 370 °C and at around 770 °C, were detected. The low temperature peak was due to the reduction of the ceria surface, while at high temperature the reduction of the bulk takes place.[49]

According to the literature,[18,44,50,51] the following assignments for the reduction of Co_3O_4 can be made: small peaks below 200 °C are attributed to the reduction of surface oxygen species adsorbed on oxygen vacancies; peaks in the range 240–320 °C are due to the reduction of Co^{3+} to Co^{2+} for Co_3O_4 at the interface with CeO_2; between 320–480 °C reduction in a single step of Co_3O_4 to Co occurs for isolated clusters not interacting with ceria; and finally, in the range 480–700 °C reduction of Co^{2+} to Co^0 is accomplished for CoO_x species interacting with ceria.

Moreover, it is likely that ceria reduction is in turn promoted by interaction with Co_3O_4 and therefore surface reduction could overlap with Co^{3+} to Co^{2+} reduction, while the bulk reduction of isolated ceria (not strongly interacting with Co_3O_4) takes place at around 740 °C. The so far listed assignments of reduction peaks are supported by the hydrogen consumptions listed in Table 2. The total consumption was comparable within the experimental error for all Co30Ce samples; however, different volumes were consumed in the three ranges of temperature identified in Table 2.

For the $Co30Ce_{urea350}$ sample the low-temperature peak corresponds to 41 ml H_2 g^{-1} that exceeds the theoretical value of about 30 ml g^{-1} (calculated at 1 atm and 298 K) expected for the reduction of Co^{3+} to Co^{2+}. Only a very small hydrogen consumption was observed in the range 300–400 °C (0.8 ml g^{-1}), while the hydrogen consumed between 400–550 and 680–820 °C accounts for the reduction of Co^{2+} to Co^0 and for the bulk reduction of ceria. On this basis, it could be inferred that in $Co30Ce_{urea350}$ ceria surface reduction occurs between 100–300 °C overlapping with Co^{3+} reduction. Moreover, on the basis of the values in Table 2 and in agreement with our previous findings[20] it appears that Co_3O_4 nanoparticles finely dispersed over ceria catalyse the reduction of the bulk CeO_2 at temperature as low as 400–550 °C. On the other hand the good dispersion of Co_3O_4 nanoclusters at the interface with ceria and the absence of the independent bulk-like Co_3O_4

Table 2 H_2 uptakes and relative Co^{3+} contents of the Co30Ce catalysts prepared by the precipitation method using three different precipitating agents and calcined at 350 or at 650 °C

	Range of temperature (°C)				
	100–300	300–400	400–550	680–820	
Sample	V^a (ml g^{-1})				$V_{total}{}^a$ (ml g^{-1})
$Co30Ce_{urea350}$	41.0	0.8	102.0	2.5	146.3
$Co30Ce_{Na350}$	45.0	98.0		4.0	147.0
$Co30Ce_{NH_4350}$	21.0	118.0		5.7	144.7

	Range of temperature (°C)			
	200–380	400–500	680–820	
Sample	V^a (ml g^{-1})			$V_{total}{}^a$ (ml g^{-1})
$Co30Ce_{urea650}$	133.0	4.0	12.0	149.0
$Co30Ce_{Na650}$	125.0	8.5	13.0	146.5
$Co30Ce_{NH_4650}$	124.0	9.5	14.0	147.5

[a] All values were calculated at 1 atm and 298 K.

phase were further confirmed by the very low intensity of the peak in the range of 300–400 °C.[18] The small peak at around 740 °C, corresponding to 2.5 ml H_2 g^{-1}, has been assigned to the reduction of a few isolated ceria clusters.

The explanation for the reduction profile of $Co30Ce_{Na350}$ is the same as for $Co30Ce_{urea350}$, although some differences emerge from a careful examination of Fig. 9c: the first reduction peak (at 275 °C) is shifted to higher temperature with respect to $Co30Ce_{urea350}$; moreover in the range 300–400 °C surface reduction of ceria, not interacting with Co_3O_4, occurs.

On the other hand, for $Co30Ce_{NH_4350}$, in the range of temperature between 300–400 °C, the contribution to the reduction profile of the ceria surface and as well of isolated Co_3O_4 crystallites is much more pronounced than for the previous samples.

These findings suggest that for Co30Ce oxides the mean crystallite size of the Co_3O_4 phase is not the only parameter influencing the reduction profile; in fact the Co_3O_4–CeO_2 interaction seems to prevail.

For Co30Ce samples calcined at 650 °C, reduction features typical of Co_3O_4, surface and bulk CeO_2 were singly detected (Fig. 9d). Co_3O_4 reduction was achieved in the range 200–380 °C; surface and bulk ceria reduction occurred at around 400–440 °C and at about 740 °C, respectively. The hydrogen consumptions listed in Table 2 are consistent with the above assignments. The presence of two reduction peaks at low temperature detected only for $Co30Ce_{urea650}$ is in agreement with the presence of relatively small Co_3O_4 crystallites that are reduced through a two-step process. Moreover, the hydrogen consumption registered for such a sample between 200–380 °C is higher than the theoretical one expected for the complete reduction of 30 wt% Co_3O_4 to metallic cobalt (~122 ml H_2 g^{-1} calculated at 1 atm and 298 K), suggesting that some ceria surface reduction is overlapping with the reduction process from Co^{3+} to Co^{2+} to Co^0.

Conversely, isolated clusters not interacting with CeO_2 and/or larger Co_3O_4 crystallites, such as those detected for $Co30Ce_{Na650}$ and $Co30Ce_{NH_4650}$, give rise to TPR curves quite similar to those of the bare Co_3O_4 samples calcined at the same temperature. Reduction of surface and bulk ceria occurred with two distinct peaks between 400–500 °C and 680–820 °C.

3.3. X-ray Photoelectron Spectroscopy (XPS)

In order to gain more insight into the surface chemical composition of Co30Ce oxides as a function of the preparation method and calcination temperature, XPS analyses were carried out on samples calcined at 350 and 650 °C. The data in terms of Co 2p and Ce 3d binding energies, Co/Ce atomic ratio and relative surface content of Co^{3+} are summarized in Table 3. For all samples, no extra detectable peaks due to impurities, like residual sodium ions, were observed. For all Co30Ce samples, the Co 2p XP spectra exhibited two main peaks at about 795.0 ± 0.2 and 780.0 ± 0.3 eV corresponding to the Co $2p_{1/2}$ and Co $2p_{3/2}$ spin–orbital peaks, respectively. For the mixed valence Co_3O_4 a spin–orbit splitting value of

Table 3 XPS data for the Co30Ce catalysts prepared by the precipitation method using three different precipitating agents and calcined at 350 or at 650 °C

Sample	Co $2p_{3/2}$ (eV)	Ce $3d_{5/2}$ (eV)	Surface Co/Ce atomic ratio[a]	$Co^{3+}/(Co^{3+} + Co^{2+})$ (%)
$Co30Ce_{urea350}$	779.9	882.0	6.3	47.0
	781.3	884.4		
$Co30Ce_{Na350}$	779.6	882.2	3.8	46.0
	781.8	884.6		
$Co30Ce_{NH_4350}$	779.6	882.2	1.8	45.0
	780.9	884.6		
$Co30Ce_{urea650}$	779.7	882.4	4.3	45.0
	781.5	884.8		
$Co30Ce_{Na650}$	779.9	882.4	1.5	48.0
	781.7	884.8		
$Co30Ce_{NH_4650}$	780.1	881.9	0.8	47.0
	782.0	884.3		

[a] The nominal value of Co/Ce is equal to 0.92.

15.2 eV has been reported.[18,20,45] Here the spin–orbit value is 15.0 ± 0.1 eV close to that of Co_3O_4. Moreover, the shake-up satellite with a low intensity at *ca.* 7.0 eV from the main Co $2p_{3/2}$ spin–orbit components is also characteristic of pure Co_3O_4.[52] In Fig. S5† experimental and fitted XP spectra of two selected samples, $Co30Ce_{urea350}$ and $Co30Ce_{NH_4350}$, are displayed as an example and are also representative of the other samples.

As observed from the Co $2p_{3/2}$ binding energies listed in Table 3, no change in the oxidation state of cobalt induced by the precipitation agent or by the calcination temperature was observed for the Co30Ce series. The relative surface content of Co^{3+} ($Co^{3+}/(Co^{3+} + Co^{2+})$ (%)) was ~46% for all samples and this value was higher than that reported for the analogous Co_3O_4/ZSM-5 systems.[53] The results in Table 3 show that the precipitation agent plays an important role in the surface composition in terms of the Co/Ce atomic ratio. For instance, $Co30Ce_{Na350}$ and $Co30Ce_{NH_4350}$ have a relatively low surface Co/Ce ratio (3.8 and 1.8, respectively), while for $Co30Ce_{urea350}$ considerable cobalt enrichment (Co/Ce = 6.3) of the surface was observed. Anyhow, according to the Co_3O_4 preparation method (namely precipitation over the ceria surface), cobalt enrichment of the surface occurs and the surface atomic ratios are always higher than the nominal value (Co/Ce = 0.92). After calcinations at 650 °C, due to Co_3O_4 crystallite sintering and specific surface area shrinkage the amount of Co detected on the surface generally decreased; the decrease was less dramatic for $Co30Ce_{urea650}$.

XPS analysis was carried out also to characterize nanocrystalline ceria. The spectrum (not shown) was typical of a pure ceria spectrum[49] and was fitted with eight peaks corresponding to four pairs of spin–orbit doublets arising from the multiplicity of the final states reached during the Ce 3d photoionization process.[54] In Table 3 the $Ce3d_{5/2}$ binding energy values are listed. Interestingly, a constant $Ce^{3+}/(Ce^{4+} + Ce^{3+})$ atomic ratio equal to ~16% was found for all samples as well for the pure nanocrystalline ceria, which was analysed for comparison. This high percentage of Ce^{3+}, which was not induced by X-ray exposure as determined by recording the spectra after different exposure time, is indicative of high oxygen vacancy content likely related to the peculiar nanocrystalline structure.[20]

3.4. Methane oxidation tests

The methane oxidation activity of the bare Co_3O_4 and Co30Ce catalysts calcined at 350 °C and at 650 °C are shown in Fig. 10a–d in terms of CH_4 conversion (%) curves *versus*

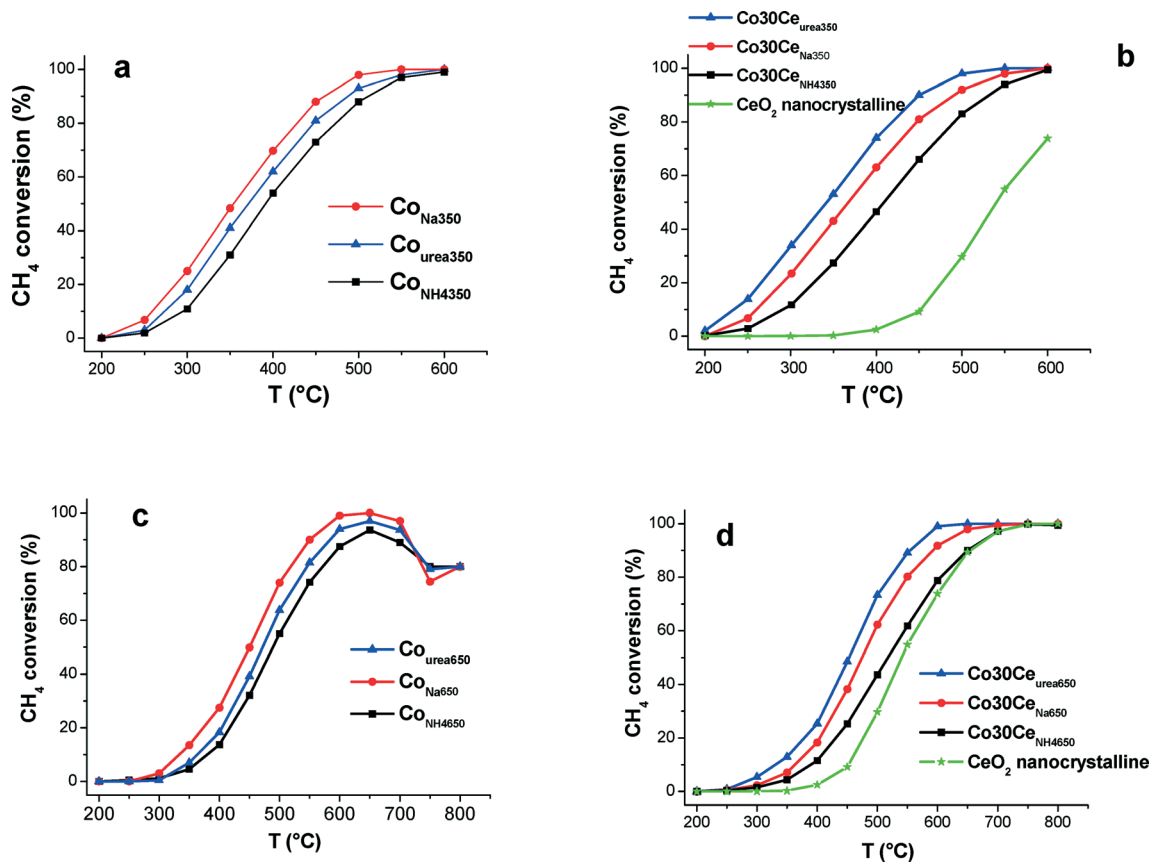

Fig. 10 CH_4 conversion curves *versus* temperature for bare Co_3O_4 and Co30Ce catalysts prepared by the precipitation method using three different precipitating agents and calcined at 350 (a, b) and at 650 °C (c, d). The CH_4 conversion curves of nanocrystalline ceria are also reported for comparison (b, c).

temperature. In Tables 4 and 5 the T_{50} and T_{90} values (the reaction temperature at which 50% or 90% methane conversion is reached) are listed for samples calcined at 350 and at 650 °C, respectively. The reaction rates (μmol CH_4 s^{-1} $g_{catalyst}^{-1}$) calculated for conversions < 20% are also reported in Tables 4 and 5. Among the Co_3O_4 oxides calcined at 350 °C and at 650 °C, the activity increased in the order Co_{NH_4} < Co_{urea} < Co_{Na}, with the latter showing the lowest T_{50} and T_{90} values for methane conversion and the highest reaction rate. XRD and BET characterization showed that Co_{Na} has smaller crystallites and a higher surface area than the other bare oxides. Moreover, the TPR reducibility decreased moving from Co_{NH_4} to Co_{Na}. These factors can account for the trend of the activity, in accordance with several literature results highlighting that the crystal size, shape and crystal orientation planes are key factors in the CH_4 oxidation activity of Co_3O_4 nanocrystals.[5,14,31]

Looking at the Co30Ce catalysts calcined at 350 °C and at 650 °C, the catalytic activity for methane oxidation increased in the order $Co30Ce_{NH_4}$ < $Co30Ce_{Na}$ < $Co30Ce_{urea}$ (Tables 4 and 5) and seems to be not only governed by the Co_3O_4 crystallite size but also by a combination of several factors, such as the homogeneous distribution and mutual interaction between Co_3O_4 and CeO_2. The key role of such a mutual interaction is not surprising considering the recent results on the peculiar structure of Co_3O_4 crystallites encapsulated by nanosized ceria that maximized the interaction between the two oxides with unique redox and catalytic properties.[18]

Table 4 Temperatures of 50 and 90% CH_4 conversion (T_{50} and T_{90}) and reaction rates (r) calculated at 250 °C (conversions < 20%) for Co_3O_4 and Co30Ce catalysts prepared by using three different precipitating agents and calcined at 350 °C. For comparison, the values obtained for nanocrystalline ceria are also listed

Sample	T_{50} (°C)	T_{90} (°C)	r (μmol CH_4 g_{cat}^{-1} s^{-1})
Co_{urea}	371	487	0.153
Co_{Na}	354	460	0.281
Co_{NH_4}	392	512	0.098
$Co30Ce_{urea}$	343	450	0.373
$Co30Ce_{Na}$	366	490	0.215
$Co30Ce_{NH_4}$	409	531	0.102
CeO_2	526	—	0.0004

Table 5 Temperatures of 50 and 90% CH_4 conversion (T_{50} and T_{90}) and reaction rates (r) calculated at 300 °C (conversions < 20%) for Co_3O_4 and Co30Ce catalysts prepared by using three different precipitating agents and calcined at 650 °C. For comparison, the values obtained for nanocrystalline ceria are also listed

Sample	T_{50} (°C)	T_{90} (°C)	r (μmol g_{cat}^{-1} s^{-1})
Co_{urea}	472	583	0.133
Co_{Na}	449	550	0.225
Co_{NH_4}	490	623	0.082
$Co30Ce_{urea}$	451	549	0.266
$Co30Ce_{Na}$	474	593	0.156
$Co30Ce_{NH_4}$	518	649	0.082
CeO_2	526	653	0.0049

XRD and BET characterization performed on selected spent Co_{350} and $Co30Ce_{350}$ catalysts, recovered after catalytic tests performed up to 600 °C, which is higher than that of the calcination treatment, showed a slight increase of the mean crystallite size, in the same trend observed for the samples calcined at 650 °C, without any dramatic structural and morphological change.

The catalytic data for the Co series and Co30Ce samples herein described are in good agreement with our previous results[20,21] recorded under the same WHSV conditions on precipitated Co_3O_4 and Co30Ce oxides with a comparable crystallite size and surface area. By comparison with other literature results[31] the present Co_3O_4 catalysts apparently have lower performance (0.225 μmol g_{cat}^{-1} s^{-1} at 300 °C for Co_{Na650}) than the Co_3O_4 nanocrystals synthesized *via* a hydrothermal process and characterized by different shapes, like nanosheets, nanobelts and nanocubes (0.544, 0.424 and 0.359 μmol g_{cat}^{-1} s^{-1}, respectively, calculated at 273–284 °C). The superior catalytic activity of such pure Co_3O_4 nanocrystals may be correlated with the more reactive crystal planes exposed on their surface. On the other hand, different specific rates of methane conversion may depend on different experimental conditions (WHSV = 60 000 ml g^{-1} h^{-1} in the present case, GHSV = 40 000 h^{-1} (ref. 31)).

For methane oxidation on cobalt oxide-based catalysts, a number of parameters, such as the crystallite size, specific surface area, reducibility of the cobalt species, nature of the support and the cobalt content on the surface, are thought to influence the catalytic activity.[20,21,53]

In Fig. 11a–b, the reaction rates (μmol CH_4 s^{-1} $g_{catalyst}^{-1}$) *versus* Co_3O_4 wt% and *versus* the Co/Ce XPS atomic ratio are displayed for the Co and Co30Ce samples. The precipitation agent and calcination temperature seriously influenced the catalytic activity. Besides the samples precipitated by $(NH_4)_2CO_3$ showing relatively low activity and performing similarly, the activity of bare Co_3O_4 and Co30Ce oxides precipitated with the same agent significantly differed as a function of the calcination temperature and Co/Ce surface atomic ratio. The highest activity was registered for the Co30Ce oxides prepared by urea according to the high reducibility observed at low temperature (Fig. 9) as well to the homogeneous distribution of the small Co_3O_4 particles over CeO_2 strongly interacting with them (Fig. 8).

In accordance with the literature, the combustion of methane over the cobalt oxide catalyst follows a Mars–van Krevelen mechanism and depends on the fast migration of oxygen ions through the lattice of cobalt oxide.[53] Thus, the oxygen buffer by release/uptake of oxygen through redox processes involving the Ce^{4+}/Ce^{3+} couple contributed to the methane oxidation at high temperature. Accordingly, nanocrystalline ceria showed appreciable activity starting from about 450 °C giving 50% methane conversion at 526 °C and an almost full conversion at 700 °C (see Table 5 and Fig. 10d). Moreover, stable methane conversions were registered for all Co30Ce catalysts above 700 °C although it is well known that at high temperature, the active phase,

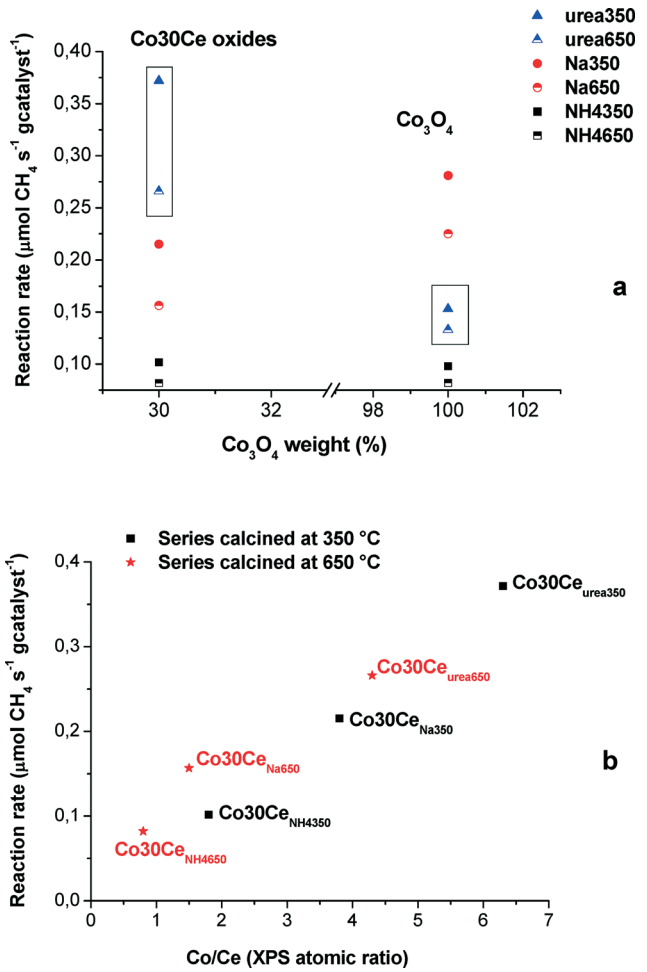

Fig. 11 (a), (b) Reaction rates (μmol CH_4 s^{-1} $g_{catalyst}^{-1}$) of Co_3O_4 and the Co30Ce series calcined at 350 °C and at 650 °C *vs.* (a) Co_3O_4 weight (%) and (b) Co/Ce (XPS atomic ratio).

Co_3O_4, partially decomposes to the less active CoO oxide.[20,21] In the present case, the attainment of stable catalytic conversions is likely due to the co-catalytic effect of CeO_2 at 700 °C (see Fig. 10d). On the other hand, for bare Co_3O_4 catalysts an evident CH_4 conversion decay was observed above 700 °C (see Fig. 10c–d). Except for the appearance of the CoO phase detected in the XRD patterns of the spent Co650 and $Co30Ce_{650}$ catalysts recovered after the catalytic tests performed at 800 °C, no sintering phenomena or morphological changes were noticed suggesting good stability under the reaction conditions for the samples calcined at 650 °C for 5 h.

3.5. Temperature-programmed desorption of NH_3

The key role of surface Lewis acidity of nanocrystalline Co_3O_4 oxides in the catalytic oxidation of chlorinated VOCs has been recently demonstrated.[55] A high Lewis acidity evaluated by means of NH_3-TPD analysis was found to be relevant to the promotion of the conversion of 1,2-dichloroethane.

Moreover, Qiu *et al.* have proposed a close relationship between the catalytic activity of catalysts for SCR and the surface adsorption level of NH_3.[48] A direct proportion between the NH_3 adsorption capacity and the abundance of Co^{3+} on the surface of Co_3O_4 nanocatalysts was found.

A linear relationship between the specific reaction rates of methane conversion and Co/Ce surface atomic ratio (Fig. 11b) has been reported, confirming our previous results on the catalytic role of the Co^{3+} species in methane oxidation activity.[20–23] In order to gain further insight into the influence of Lewis acidity on the catalytic performance of Co_3O_4–CeO_2 systems, NH_3-TPD experiments were carried out over selected samples, Co_3O_4 and Co30Ce calcined at 350 and at 650 °C. Nanocrystalline ceria has been tested for comparison. Some representative NH_3-TPD profiles are displayed in Fig. 12. The total acidity values expressed as mmol of desorbed NH_3 per gram of the catalyst and calculated by integrating the area under the TPD curves are listed in Table 6. The most intense features were observed for $Co30Ce_{urea350}$ showing a broad peak between 150–350 °C and a second and less intense signal extended to the entire holding time at 500 °C. In accordance with the literature,[55] peaks at $T \leq 200$ °C can be attributed to the presence of weak acid sites, while desorption occurring between 300–500 °C is associated with strong acid sites. The desorption profile of $Co_{urea350}$ is characterized by a very large and continuous peak in the range 200–500 °C, suggesting also in this case the presence of both weak and strong acid sites. However, by comparing the two curves of $Co_{urea350}$ and $Co30Ce_{urea350}$ it is evident that the abundance and strength of the acid sites of pure Co_3O_4 strongly differed from those of the corresponding Co_3O_4–CeO_2 oxide that in turn is much more acidic than the parent CeO_2. These findings suggest that the deposition over ceria of regular and highly dispersed Co_3O_4 nanoparticles by precipitation with urea is an effective method to form abundant Co^{3+} ions responsible for the high NH_3 adsorption capacity. In contrast to $Co30Ce_{urea350}$, the acid capacity of

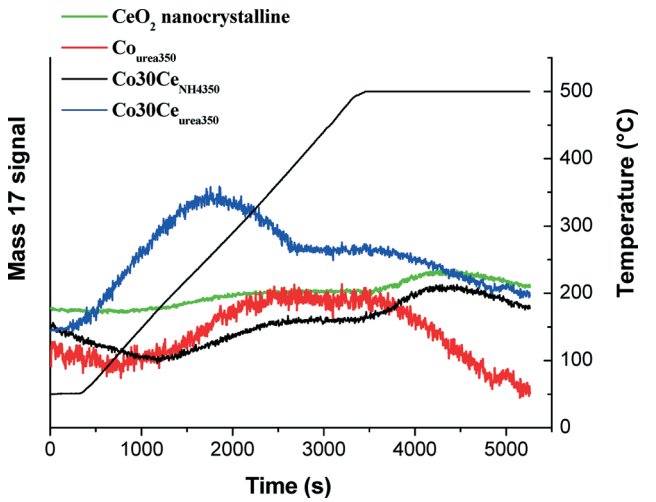

Fig. 12 NH_3-TPD profiles of selected Co30Ce and Co_3O_4 oxides calcined at 350 °C. The curve for nanocrystalline CeO_2 is reported for comparison.

Table 6 NH_3-TPD data for selected Co_3O_4 and Co30Ce catalysts prepared by using three different precipitating agents and calcined at 350 and at 650 °C. For comparison, the values calculated for nanocrystalline ceria are also listed

Samples	Total acidity (mmol NH_3 g_{cat}^{-1})
$Co_{urea350}$	0.21
$Co30Ce_{urea350}$	0.35
$Co30Ce_{NH_4350}$	0.19
CeO_2	0.09
$Co_{urea650}$	0.14
$Co30Ce_{urea650}$	0.26
$Co30Ce_{NH_4650}$	0.10

$Co30Ce_{NH_4350}$ was much lower. The acidity decreased for all samples after calcination at 650 °C (see Table 6), in agreement with Co_3O_4 crystallite sintering generally observed for bare oxides and Co30Ce samples. $Co30Ce_{urea650}$ was the sample that preserved a larger amount of acid sites.

Conclusions

The synthetic procedure, precipitation by $(NH_4)_2CO_3$, Na_2CO_3 and $CO(NH_2)_2$, influenced the nature of the cobalt species as determined by XRD characterization of powders dried at 120 °C (formation of cobalt hydroxide carbonate or the Co_3O_4 spinel species).

Upon calcination at 350 °C cobalt crystallized into the pure Co_3O_4 spinel phase for all samples, regardless of the precipitation agent and chemical composition. Textural (crystallite size and specific surface area) and catalytic properties strongly depend on the nature of the precipitation agent. Homogeneous precipitation by Na_2CO_3 and $CO(NH_2)_2$ led to regular and controlled Co_3O_4 particle sizes, while bigger and heterogeneous crystals were formed with $(NH_4)_2CO_3$. When the precipitation of cobalt oxides was carried out in the presence of ceria by sodium or ammonium carbonate, the sample mapping carried out by TEM and SEM analyses appears to be quite heterogeneous, with large agglomerations of CeO_2 particles, which are not directly interacting with the Co_3O_4 crystallites. This effect is more evident in the case of the sample precipitated by $(NH_4)_2CO_3$ characterized by big Co_3O_4 crystallites. In contrast, homogeneous precipitation *via* urea appears to be the most adequate method for preparing regular nanocrystalline Co_3O_4 particles homogeneously distributed over ceria and strongly interacting with them.

The peculiar structure and morphology of nanocrystalline ceria play a fundamental role in stabilizing the Co_3O_4 active phase against sintering and promoting its activity. This trend was common to all Co_3O_4–CeO_2 mixed oxides.

The excellent catalytic activity of the Co_3O_4–CeO_2 catalyst precipitated by urea can be attributed to a combination of several factors, such as the small crystallite size which gives rise to easily accessible active sites, easy reducibility of Co^{3+} at low temperature, and high surface Co^{3+} content at the Co_3O_4–CeO_2 interface. The mutual interaction between the two oxides guarantees full methane conversion above 700 °C.

Acknowledgements

The authors acknowledge the financial support provided by the Network of Excellence IDECAT (Integrated Design of Catalytic Nanomaterials for a Sustainable Production) and by the COST Action CM 1104.

The authors are sincerely grateful to Prof. A. Corma of the Instituto de Tecnologia Quimica (CSIC-UPV), University Politecnica de Valencia for valuable suggestions and discussion.

Dr. Francesco Giordano of ISMN-CNR is acknowledged for XRD analyses.

The China Scholarship Council is sincerely acknowledged for supporting Wu's and Guo's scholarships. H. Wu and S. Guo thank the Excellent Doctorate Foundation, the Doctorate Foundation of Northwestern Polytechnical University and the Scholarship Award for Excellent Doctoral Student granted by the Ministry of Education, P.R. China.

References

1 J. J. Spivey, *Ind. Eng. Chem. Res.*, 1987, **26**, 2165–2180.
2 M. M. Zwinkels, S. G. Jaras and P. G. Menon, *Catal. Rev.: Sci. Eng.*, 1993, **35**, 319–358.
3 J. Jansson, *J. Catal.*, 2000, **194**, 55–60.
4 V. G. Milt, M. A. Ulla and E. A. Lomardo, *Catal. Lett.*, 2000, **65**, 67–73.
5 T.-C. Xiao, S.-F. Ji, H.-T. Wang, K. S. Coleman and M. L. H. Green, *J. Mol. Catal. A: Chem.*, 2001, **175**, 111–123.
6 J. Kirchnerova, M. Alifanti and B. Delmon, *Appl. Catal., A*, 2002, **231**, 65–80.
7 M. Kang, M. W. Song and C. H. Lee, *Appl. Catal., A*, 2003, **251**, 143–156.
8 C.-W. Tang, C.-C. Kuo, M.-C. Kuo, C.-B. Wang and S.-H. Chien, *Appl. Catal., A*, 2006, **309**, 37–43.
9 C.-W. Tang, M.-C. Kuo, C.-J. Lin, C.-B. Wang and S.-H. Chien, *Catal. Today*, 2008, **131**, 520–525.
10 J. Łojewska, A. Kołodziej, T. Łojewski, R. Kapica and J. Tyczkowski, *Appl. Catal., A*, 2009, **366**, 206–211.
11 X. Xie, Y. Li, Z.-Q. Liu, M. Haruta and W. Shen, *Nature*, 2009, **458**, 746–749.
12 V. G. Milt, C. A. Querini, E. E. Miró and M. A. Ulla, *J. Catal.*, 2003, **220**, 424–432.
13 M. Dhakad, T. Mitshulhashi, S. Rayalu, P. Doggali, S. Bakardjiva, J. Subrt, D. Fino, H. Haneda and N. Labhsetwar, *Catal. Today*, 2008, **132**, 188–193.
14 U. Zavyalova, P. Scholz and B. Ondruschka, *Appl. Catal., A*, 2007, **323**, 226–233.
15 J. Li, X. Liang, S. Xu and J. Hao, *Appl. Catal., B*, 2009, **90**, 307–312.
16 M. M. Natile and A. Glisenti, *Chem. Mater.*, 2005, **17**, 3403–3414.
17 Xue Li, C. Zhang, H. He and Y. Teraoka, *Appl. Catal., B*, 2007, **75**, 167–174.
18 J.-Y. Luo, M. Meng, X. Li, X.-G. Li, Y.-Q. Zha, T.-D. Hu, Y.-N. Xie and J. Zhang, *J. Catal.*, 2008, **254**, 310–324.

19 C.-W. Tang, W.-Y. Yu, C.-J. Lin, C.-B. Wang and S.-H. Chien, *Catal. Lett.*, 2007, **116**, 161–166.
20 L. F. Liotta, G. Di Carlo, G. Pantaleo, A. M. Venezia and G. Deganello, *Appl. Catal., B*, 2006, **66**, 217–227.
21 L. F. Liotta, G. Di Carlo, G. Pantaleo and G. Deganello, *Appl. Catal., B*, 2007, **70**, 314–322.
22 L. F. Liotta, M. Ousmane, G. Di Carlo, G. Pantaleo, G. Deganello, G. Marcì, L. Retailleau and A. Giroir-Fendler, *Appl. Catal., A*, 2008, **347**, 81–88.
23 L. F. Liotta, M. Ousmane, G. Di Carlo, G. Pantaleo, G. Deganello, A. Boreave and A. Giroir-Fendler, *Catal. Lett.*, 2009, **127**, 270–276.
24 L. F. Liotta, G. Pantaleo, A. Macaluso, G. Di Carlo and G. Deganello, *Appl. Catal., A*, 2003, **245**, 167–177.
25 I. Yu. Zavaliy, R. V. Denys, R. Cerny, I. V. Koval'chuk, G. Wiesinger and G. Hilscher, *J. Alloys Compd.*, 2005, **386**, 26–34.
26 S. Carrettin, P. Concepción, A. Corma, J. M. L. Nieto and V. F. Puntes, *Angew. Chem., Int. Ed.*, 2004, **43**, 2538–2540.
27 J. Guzman, S. Carrettin and A. Corma, *J. Am. Chem. Soc.*, 2005, **127**, 3286–3287.
28 T. Ishikawa and E. Matijević, *Colloid Polym. Sci.*, 1991, **269**, 179–186.
29 R. Xu and H. C. Zeng, *J. Phys. Chem. B*, 2003, **107**, 12643–12649.
30 B. Li, Y. Xie, C. Wu, Z. Li and J. Zhang, *Mater. Chem. Phys.*, 2006, **99**, 479–486.
31 L. Hu, Q. Peng and Y. Li, *J. Am. Chem. Soc.*, 2008, **130**, 16136–16137.
32 S. J. Gregg and K. S. Sing, *Adsorption, Surface Area and Porosity*, Academic Press, San Diego, 2nd edn, 1982.
33 *Inorganic Crystal Structure Database*, ICSD, FIZ Karlsruhe, 2014.
34 H. P. Klug and L. E. Alexander, *X-ray Diffraction Procedures for Polycrystalline and Amorphous Materials*, Wiley, New York, 1954.
35 D. A. Shirley, *Phys. Rev. B: Solid State*, 1972, **5**, 4709–4714.
36 P. M. A. Sherwood, *Practical Surface Analysis*, ed. D. Briggs and M. P. Seah, Wiley, New York, 1990, p. 181.
37 T. Baird, K. C. Campbell, P. J. Holliman, R. W. Hoyle, D. Stirling, B. P. Williams and M. Morris, *J. Mater. Chem.*, 1997, **7**, 319.
38 V. G. Hadjiev, M. N. Iliev and I. V. Vergilov, *J. Phys. C: Solid State Phys.*, 1988, **21**, L199–L201.
39 C. W. Tang, C. B. Wang and S. H. Chein, *Thermochim. Acta*, 2008, **473**, 68–73.
40 H.-H. Chou and H. Y. Fan, *Phys. Rev. B: Solid State*, 1976, **13**, 3924–3938.
41 J. Liu, Z. Zhao, J. Wang, C. Xu, A. Duan, G. Jian and Q. Yang, *Appl. Catal., B*, 2008, **84**, 185–195.
42 L. F. Liotta, H. J. Wu, G. Pantaleo and A. M. Venezia, *Catal. Sci. Technol.*, 2013, **3**, 3085–3102.
43 P. Arnoldy and J. A. Moulijn, *J. Catal.*, 1985, **93**, 38–54.
44 J. Y. Luo, M. Meng, Y. Q. Zha and L. H. Guo, *J. Phys. Chem. C*, 2008, **112**, 8694–8701.
45 Q. Y. Yan, X. Y. Li, Q. D. Zhao and G. H. Chen, *J. Hazard. Mater.*, 2012, **209–210**, 385–391.
46 G. Jacobs, Y. Y. Ji, B. H. Davis, D. Cronauer, A. J. Kropf and C. L. Marshall, *Appl. Catal., A*, 2007, **333**, 177–191.
47 A. Y. Khodakov, A. G. Constant, R. Bechara and F. Villain, *J. Phys. Chem. B*, 2001, **105**, 9805–9811.
48 B. Meng, Z. K. Zhao, X. Z. Wang, J. J. Liang and J. S. Qiu, *Appl. Catal., B*, 2013, **129**, 491–500.
49 A. M. Venezia, G. Pantaleo, A. Longo, G. Di Carlo, M. P. Casaletto, L. F. Liotta and G. Deganello, *J. Phys. Chem. B*, 2005, **109**, 2821–2827.
50 C. W. Tang, C. C. Kuo, M. C. Kuo, C. B. Wang and S. H. Chien, *Appl. Catal., A*, 2006, **309**, 37–43.
51 W. Song, A. S. Poyraz, Y. Meng, Z. Ren, S.-Y. Chen and S. L. Suib, *Chem. Mater.*, 2014, **26**, 4629–4639.
52 H. J. Wu, L. D. Wang, Z. Y. Shen and J. H. Zhao, *J. Mol. Catal. A: Chem.*, 2011, **351**, 188–195.
53 Z. Z. Zhu, G. Z. Lu, Z. G. Zhang, Y. Guo, Y. L. Guo and Y. Q. Wang, *ACS Catal.*, 2013, **3**, 1154–1164.
54 A. Pfau and K. D. Schierbaum, *Surf. Sci.*, 1994, **321**, 71–80.
55 B. de Rivas, R. López-Fonseca, C. Jiménez-González and J. I. Gutiérrez-Ortiz, *J. Catal.*, 2011, **281**, 88–97.

